Traction Stresses and Translational Distortion of the Nucleus During Fibroblast Migration on a Physiologically Relevant ECM Mimic

Zhi Pan,[†] Kaustabh Ghosh,[‡] Yajie Liu,[§] Richard A. F. Clark,[¶*] and Miriam H. Rafailovich[†*]
[†]Department of Materials Science and Engineering, [‡]Department of Biomedical Engineering, [§]Department of Mechanical Engineering, and [¶]Department of Biomedical Engineering, Dermatology and Medicine, State University of New York at Stony Brook, Stony Brook, New York

ABSTRACT Cellular traction forces, resulting in cell-substrate physical interactions, are generated by actin-myosin complexes and transmitted to the extracellular matrix through focal adhesions. These processes are highly dynamic under physiological conditions and modulate cell migration. To better understand the precise dynamics of cell migration, we measured the spatio-temporal redistribution of cellular traction stresses (force per area) during fibroblast migration at a submicron level and correlated it with nuclear translocation, an indicator of cell migration, on a physiologically relevant extracellular matrix mimic. We found that nuclear translocation occurred in pulses whose magnitude was larger on the low ligand density surfaces than on the high ligand density surfaces. Large nuclear translocations only occurred on low ligand density surfaces when the rear traction stresses completely relocated to a posterior nuclear location, whereas such relocation took much longer time on high ligand density surfaces, probably due to the greater magnitude of traction stresses. Nuclear distortion was also observed as the traction stresses redistributed. Our results suggest that the reinforcement of the traction stresses around the nucleus as well as the relaxation of nuclear deformation are critical steps during fibroblast migration, serving as a speed regulator, which must be considered in any dynamic molecular reconstruction model of tissue cell migration. A traction gradient foreshortening model was proposed to explain how the relocation of rear traction stresses leads to pulsed fibroblast migration.

INTRODUCTION

Cell migration plays an important role in many normal and pathological processes, ranging from tissue morphogenesis and regeneration to wound healing and tumor metastasis. As a result, a great deal of research has already been done trying to understand the process. There is general agreement that cell migration consists of a series of coordinated steps: lamellipodium extension at the leading edge, adhesion site formation behind the leading edge, and disruption of older adhesion sites at the trailing edge with concomitant retraction of the cell rear (1,2). Cellular traction forces are exerted or dissipated as these focal adhesion sites assemble or disassemble (3,4). Real-time imaging of fluorescent focal adhesion components has shown that the distribution of focal adhesions occurs mostly at the trailing edge, and it remains constant at the front of the cell (5,6). It was postulated that the cells undergo a ''clutch'' type of motion, with the focal adhesions at the cell rear dictating when motion would occur. Although such studies have successfully revealed the critical role of focal adhesion dynamics in cell migration, they have essentially been qualitative in nature. To unequivocally confirm such models of cell migration, it is crucial to obtain rigorous and direct measurements of the dynamics of cellular traction forces that result from the redistribution of focal adhesions.

With fluorescent beads or micropatterned posts serving as randomly distributed or uniform arrays of markers on the surface of flexible substrates (7), traction force distribution of individual cells can be measured by quantifying the reversible substrate deformation (8–10) or postdeflection (11,12) caused by cell attachment. Using these techniques, several groups have measured the static distribution of traction forces involved in cell adhesion. However, fewer studies have been performed whereby the dynamics of traction forces were measured. Using time-lapse analysis of the deformation of collagen-coated polyacrylamide gels (13) produced by NIH 3T3 fibroblasts, Munevar et al. (14) were able to correlate changes in the traction stress distribution pattern with changes in the direction of cell migration. But, because the cell mobility in their cell-substrate system was very small, they were not able to resolve actual temporal redistribution of the individual traction forces that eventually leads to cell motion. du Roure et al. (15) imaged, as a function of time, the deformation of posts imprinted in a polydimethylsiloxane gel by epithelial cells. In this study, the resolution was limited by the position of the posts and by the fact that the cells were forced to adhere in the areas of the posts. Hence in contrast to previous studies on planar surfaces (9,10,16), they found that the maximum traction forces were always localized on the edge of the cell. Even though each of these studies addressed a different fundamental aspect of cell migration, neither imaged the coordinated sequence of events that ultimately resulted in the locomotion of the entire cell.

In this work, we report the use of a functionalized hydrogel, which was developed to be a physiologically relevant extracellular matrix (ECM) mimic (17), and tuned to achieve large cellular traction forces with significant cell locomotion during a convenient observation time window. We also show

Submitted July 7, 2008, and accepted for publication February 17, 2009.

*Correspondence: miriam.rafailovich@sunysb.edu; richard.clark@sunysb.edu

Editor: Elliot L. Elson.

0006-3495/09/05/4286/13 $2.00

doi: 10.1016/j.bpj.2009.02.039

that it is possible to apply the digital image speckle correlation (DISC) technique combined with finite element method (FEM) to analyze the redistribution of cellular traction stresses using standard software. This technique allows us to observe in real time the redistribution of cellular traction stresses during cell migration with high spatial resolution. Furthermore, because our technique can be adapted to any hydrogel or other flexible substrates, a wide variety of physiologically relevant constructs can be studied to obtain fundamental insights into cell dynamics on different types of tissues.

Here we chose to use intermolecularly cross-linked thiol-modified hyaluronan (HA-DTPH) functionalized with specific fibronectin functional domains (FNfds) (18) to study the migration mechanics of primary adult human dermal fibroblasts (AHDFs). Using this system, Ghosh et al. (17) had previously shown that the traction stresses exerted by cells were a sensitive function of the modulus of the substrate, which in turn was controlled by the cross-linking density. Furthermore, significant cell migration occurred on these substrates within our observation time. Hence in this study, with appropriate substrate stiffness for AHDFs, we focused on elucidating the sequence of traction stresses that lead to nuclear translocation, an indicator of cell migration. These experiments were performed as a function of ligand density, which governs cell adhesion to the substrate and consequently influences cell mobility (19) associated with other cell responses on the gel, such as cell morphology and focal adhesion distribution (20). Low ligand density surfaces (LLDS) and high ligand density surfaces (HLDS) reflective of bulk ligand densities of 0.26 μM and 0.52 μM, respectively, were investigated. These densities allowed sufficient motilities and traction forces to clearly establish the correlation between them.

MATERIALS AND METHODS

Preparation of HA/FNfds substrates

Cysteine-tagged FNfds, C-SH, and HV-SH at equal proportions, were coupled to 4.5% (w/v) cross-linker PEGDA (Nektar Therapeutics, Huntsville, AL) in PBS to form PEGDA-FNfd conjugates with different total ligand density, 0.26 μM and 0.52 μM for LLDS and HLDS, respectively. Then these conjugates were mixed with 1.25% (w/v) HA-DTPH (gift from Glenn D. Prestwich's lab, University of Utah, Salt Lake City, UT) in SF-DMEM (Sigma, St. Louis, MO) with volume ratio 1:4. The mixtures were seeded in 35 mm tissue culture dishes to gel. Fluorescent beads with 40 nm diameter (Molecular Probes, Eugene, OR) were sonicated and suspended uniformly at a concentration of 5% (v/v) in HA solution before gelation and served as markers for substrate deformation measurements. All the substrates were stored at 4°C for >18 h to stabilize PEGDA-mediated cross-linking before cells seeding.

Characterization of substrates

In the final gel, HA-DTPH and cysteine-tagged FNfds were cross-linked to PEGDA, which ensure stable mechanical and adhesive properties of the substrate. The mechanical property of the substrate was adjusted to be physiologically relevant as used in previous in vivo experiment to promote wound healing (18) with a shear storage modulus $G' = 4.27$ kPa (21) measured by an AR2000 rheometer (TA Instruments). This stiffness was also shown as the optimal rigidity for AHDFs to form normal cytoskeleton organization and to generate robust tractions for cell proliferation and migration (17). The central cell binding domain (FNIII8-11 or C) and the Heparin II binding domain including the type III connecting strand (FNIII12-V15 or HV) of fibronectin, which together are sufficient for optimal AHDF migration (22), were tethered in equal proportions to the HA hydrogel as ligands for cell adhesion. Substrate adhesiveness could be varied by changing the total ligand density without changing the stiffness of the gel (17).

Cell culture and seeding

Primary dermal fibroblasts obtained from a 31-year-old Caucasian female (Clonetics, San Diego, CA) were used between passages 5 and 13. The cells were routinely cultured in DMEM, supplemented with 10% fetal bovine serum and 1% Penicillin, Streptomycin and L-glutamine (P/S/G), in a 37°C, 5% CO_2, 95% humidity incubator (Napco Scientific, Tualatin, OR). To avoid cell-cell interactions, a low density of cells ($\sim$500/cm^2) was seeded onto HA/FNfds substrate in SF-DMEM with 1% P/S/G and followed by 6 h incubation in the incubator. Before all the experiments done in atmospheric conditions, SF-DMEM was changed to CO_2-independent media (Gibco, Carlsbad, CA) with 1% P/S/G at 37°C. Only single cells were chosen to measure traction fields and nuclear translocation.

Measurement of cellular/nuclear aspect ratio, cell area, and migration speed

Time-lapse phase images of the cells were recorded every 15 min over a 1-h time window with a MetaMorph-operated CoolSNAP™ HQ camera (Universal Imaging, Downingtown, PA) attached to a Nikon DiaphotTMD inverted microscope fitted with a 37°C stage incubator and a 10× objective lens. Using MetaMorph software, aspect ratio of cells and nuclei and projected cell area were obtained from phase images by measuring both major and minor length of each cell and its nucleus or area covered by the outline of each cell. The migration speed was determined from the time-lapse images by tracking the distance covered by the center of a cell nucleus over every 15 min in 1 h. This was a carefully chosen observation window where notable fibroblast migration was observed and no corrections for instrumental stability on the microscope had to be made. To determine whether cell migration speed was a function of the observation time, it was also measured with an observation window of 2 h, and no significant difference was observed (see Fig. S1 in the Supporting Material). The sample size n used was 5 ~ 10 cells/field × 3 ~ 5 fields. Results shown in Fig. 1 (see Fig. 3) are representative of three independent experiments.

Vinculin staining and visulization

Because immunofluorescent staining of vinculin-containing focal adhesions was difficult to perform in cells plated on the hydrogels (owing to nonspecific absorption of antibodies within hydrogels that led to a high fluorescence background), we coated tissue culture dishes with low and high densities of FN, which produced surfaces that induced cell motility similar to the LLDS and HLDS of hydrogels, respectively; 35 mm tissue culture dishes filled with 2 ml 15 μg/ml or 30 μg/ml FN solutions were maintained overnight at room temperature and then blocked using 2% (w/v) bovine serum albumin (BSA) at room temperature for 2 h. Each dish was rinsed three times with PBS, and then cells were seeded at low density in serum-free DMEM and incubated at 37°C for 6 h. The cells were then fixed with 4% paraformaldehyde in PBS for 15 min, permeabilized with 0.4% Triton in PBS for 5 min, and blocked with 2% BSA in PBS for 30 min at room temperature. Focal adhesions were visualized by immunostaining for vinculin, where antivinculin primary antibody (V9131, Sigma, St. Louis, MO) was incubated with cells at 1:600 dilution

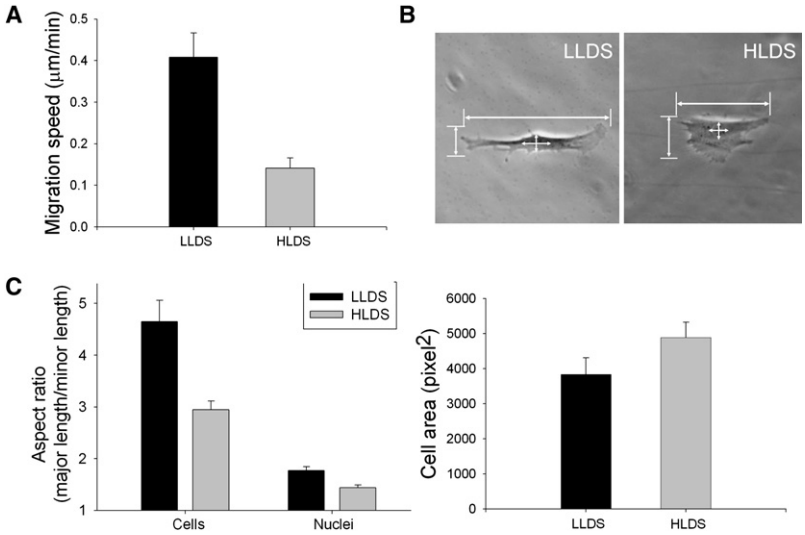

FIGURE 1 Effects of ligand density (cell-substrate adhesion) on fibroblast migration and morphology. (*A*) Mean migration speed of cells on LLDS, ($n = 26$) and on HLDS ($n = 24$). (*B*) Phase images of a typical cell on LLDS (*left*) and HLDS (*right*). The white solid lines show the major and the minor length of each cell and its nucleus. (*C*) Aspect ratio (defined as the ratio of the major to the minor length) of cells and their nuclei, and cell area on LLDS ($n = 19$) and HLDS ($n = 23$). Error bars represent SE.

for 1 h at room temperature, followed by incubation with Oregan Green 488 goat anti-mouse secondary antibody (O11033, Invitrogen, Eugene, OR) at a 1:800 dilution for 1 h. After washing, cells were kept in PBS at 4°C and imaged using a Leica TCS SP2 laser scanning confocal microscope (Leica Microsystems, Bannockburn, IL) using a 63 × NA 0.9 water objective lens. The number of vinculin-positive focal adhesions at the cell front and rear as well as across the entire cell area was quantified using ImageJ.

Measurement and calculation of cellular tractions using DISC and FEM

Quantification of cellular traction forces was accomplished by using the DISC technique combined with FEM as previously described (17), which can provide rapid and accurate measurements of cellular traction distribution with high spatial resolution. Briefly, to track deformations induced by the migrating cell, fluorescent beads were embedded in HA/FNfds hydrogel with an optimized density of 5% (v/v). After AHDFs were seeded on the substrate and incubated in SF-DMEM at 37°C for 6 h, the media was changed to CO_2-independent media before microscopy, and the whole sample was placed on a 37°C heated platform during observation. Phase contrast images of a single migrating cell and fluorescence images of the underlying (substrate-embedded) beads were recorded simultaneously every 15 min over 1 h with a differential interference contrast lens and a 63 ×, NA 0.9 water objective lens on a Leica TCS SP2 laser scanning confocal microscope (Leica Microsystems). The former provided the outline of the cell and the position of its nucleus, whereas the latter recorded the redistribution of the embedded fluorescent beads. Then images of bead positions in nonstressed gels were taken after completely detaching the cell from the substrate with the treatment of trypsin-EDTA. The confocal pinhole size was always set at optimal state so that only the beads in the top narrow layer of the substrate were recorded, and all images were recorded with a charge-coupled device camera at the same resolution of 1024 × 1024 in pixels. DISC technique was applied to compare the bead distribution change between each stressed and nonstressed image. It divided stressed image into small subsets and searched for a best match in the nonstressed image, following the equation:

$$S\left(x, y, u, v, \frac{\partial u}{\partial x}, \frac{\partial u}{\partial y}, \frac{\partial v}{\partial x}, \frac{\partial v}{\partial y}\right) = 1 - \frac{\sum I(x,y) \times I^*(x^*, y^*)}{\sqrt{\sum I(x,y)^2 \times \sum I^*(x^*, y^*)^2}}, \quad (1)$$

$x^* = x + u$, $y^* = y + v$, where (x, y) and (x^*, y^*) are the coordinates of matched subset pair; I and I^* are the intensity in corresponding subsets; and (u, v) is the coordinate difference between them, which provides the displacement vector from the position in nonstressed image to the stressed image with the best match, $S \approx 0$. The size of subset and the distance for the matched pair searching were empirically determined. The density of fluorescent beads was optimized to make sure that there are always several beads in each subset to avoid the error in calculation. Because the DISC technique utilizes the total intensity in each subset, I and I^*, to minimize the cross-correlation function (S), its resolution is independent of individual beads. Because the position of initial subset can be moved pixel by pixel, DISC technique can produce displacement data with high spatial resolution that is limited only by the resolution and size of the acquired digital image.

The time sequence of displacement data with sufficient spatial resolution was then used as the top surface boundary conditions in a long vertical cube ($209 \times 209 \times 518\ \mu m^3$) FEM model composed of 8-node three-dimensional solid elements. Standard finite element software (ABAQUS, Providence, RI) was used to perform FEM calculation. The shear stress map on top surface determined by FEM represented the cellular traction field at each time point. Different from the previous method that utilized Tikhonov regularization with a particular choice and intensity of smoothing functional (9), FEM uses no smoothing and yields an exact traction field directly based on the given displacement map. The spatial resolution is carefully chosen by considering both FEM model accuracy and its computation complexity. In this case, considering the size of the field of interest, traction fields over the whole cell were calculated from each element with nodes in every 2.3 μm along each dimension to achieve a high calculation speed, and tractions in the localized region was evaluated at nodes in every 0.70 μm (see *inset* in Fig. 5) along each dimension to gain higher resolution. The maximal traction stresses in this field were unaltered at the different resolutions tested, thus demonstrating the reliability of our method. However, higher resolution allowed better localization of the traction distribution in smaller areas. Because high-precision DISC data elucidated every single displacement on the substrate surface and no hand-drawn cell boundaries were necessary in this algorithm, all shear stresses occurring over the whole field were obtained including the background noise. Nevertheless, to emphasize the cellular tractions of interest, the background was removed from the final displayed traction field by filtering the values below a threshold defined by the average noise in each field. Because the examined cell was randomly chosen, results are representative of at least three migrating cells on LLDS and HLDS, respectively.

To quantify the strength of cell-substrate adhesion, we estimated the mechanical work done by the cell (W) from the strain energy (E) stored in the elastic substrate and calculated in the same FEM model using the equation:

$$W = E = \frac{1}{2}\int \sigma_{ij}(\bar{r}) \cdot \varepsilon_{ij}(\bar{r}) dV. \quad (2)$$

$i, j = 1, 3$.

The net stress in each subregion and the total stress over the entire cell were calculated by summing all the stress vectors in certain area of interest. These sums are proportional to the net force in subregions and the total net force, which are utilized to explain the cell motion in this study.

RESULTS

Cell migration on HA/FNfds substrates with different ligand densities

The average migration speed of single cells, cultured on LLDS or HLDS substrates for 6 h in serum free DMEM (SF-DMEM), was measured by time-lapse photography over 1 h and plotted as a histogram in Fig. 1 *A*. We found that the migration speed is nearly three times faster on LLDS than on HLDS. Fig. 1 *B* shows the morphology of typical cells on both surfaces. In Fig. 1 *C*, we plot the average aspect ratio calculated from the ratio of the major to the minor length of the cells and the nuclei shown in Fig. 1 *B*, together with the cell area. From the figure we can see that the aspect ratios of the cells and their nuclei are 40% and 23% higher, and the cell area is ~20% smaller, on LLDS than on HLDS, indicating that cell morphology and migration speed are correlated.

Because the dynamics of focal adhesions is known to influence cell polarization and migration, we monitored the number and distribution of vinculinpositive focal adhesions in cells cultured on the low and high FN density two-dimensional surfaces. Fig. 2 *A* shows fluorescent images of vinculin-positive focal adhesions in a typical cell on each substrate, whereas Fig. 2 *B* is a plot showing the quantitative comparison of the focal adhesion number and distribution between the weaker and stronger adhesive surfaces. The total number of focal adhesions per cell is an indicator of cell-substrate adhesion, whereas the ratio of focal adhesion numbers between the front and rear of a cell indicates its degree of polarization. From Fig. 2 *B*, we observe that the cells on the high FN density surface have nearly 30% more focal adhesions on average than on the low FN density surface, which scales directly with the differences in ligand density between the two surfaces. The distribution of focal adhesions, on the other hand, appears to be more asymmetric, on the low FN density surface, with more focal adhesion points at the front of the cell than at the rear (Fig. 2 *C*). Because the locus of these focal adhesions is also associated with cellular traction forces exerted on the substrate, the imbalance may also be an indicator of larger total traction stresses on the low density surface, which is consistent with the higher migration speed observed on LLDS.

In a previous report, it was shown that the locus of the focal adhesions at the rear of the cell migrated toward the interior, with a time interval of ~10 min, whereas the complexes at the front remained stationary (5). This indicates that the traction forces are readjusting over that time interval, and hence information is lost when averaging the migration speed over 1 h. We therefore divided the hour into 15 min time intervals and measured the nuclear translocation of the cells in the ensemble at the end of each interval. We then classified the nuclear translocations in every 15 min interval into three different groups, large: >10 μm, medium: 5~10 μm, and small: <5 μm. In Fig. 3 *A*, we plot the percentage of the cells that undergo small, medium, and large translocations during every 15 min intervals over 1 h. From the figure we see that the population is bimodal on the LLDS, with the percentage of cells having large translocations nearly equal to the percentage of cells having small translocations. On the HLDS though, most cells undergo small translocations. Looking further into the distribution of cells having large nuclear translocations (Fig. 3 *B*), we find that the number of large translocations in every 15 min interval over 1 h has a normal distribution for cells on LLDS, whereas most cells on HLDS have no large translocation. The average numbers of large nuclear translocation are

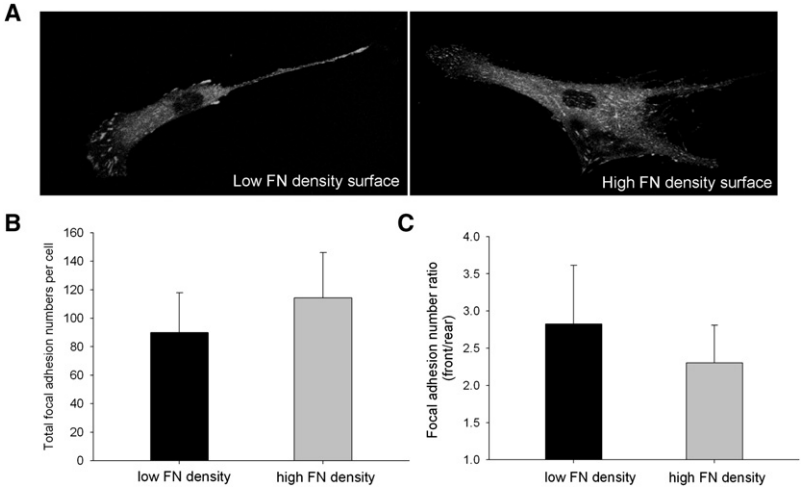

FIGURE 2 Focal adhesion distributions as a function of FN density. (*A*) Focal adhesions in cells grown on tissue culture dishes coated with low and high densities of FN, as visualized by vinculin staining. (*B*) Total number of vinculin-positive focal adhesions per cell. (*C*) Front/rear of the number of vinculin-positive focal adhesions in a cell. $n = 7$ and 9 for low and high FN density surfaces, respectively. Error bars represent SD.

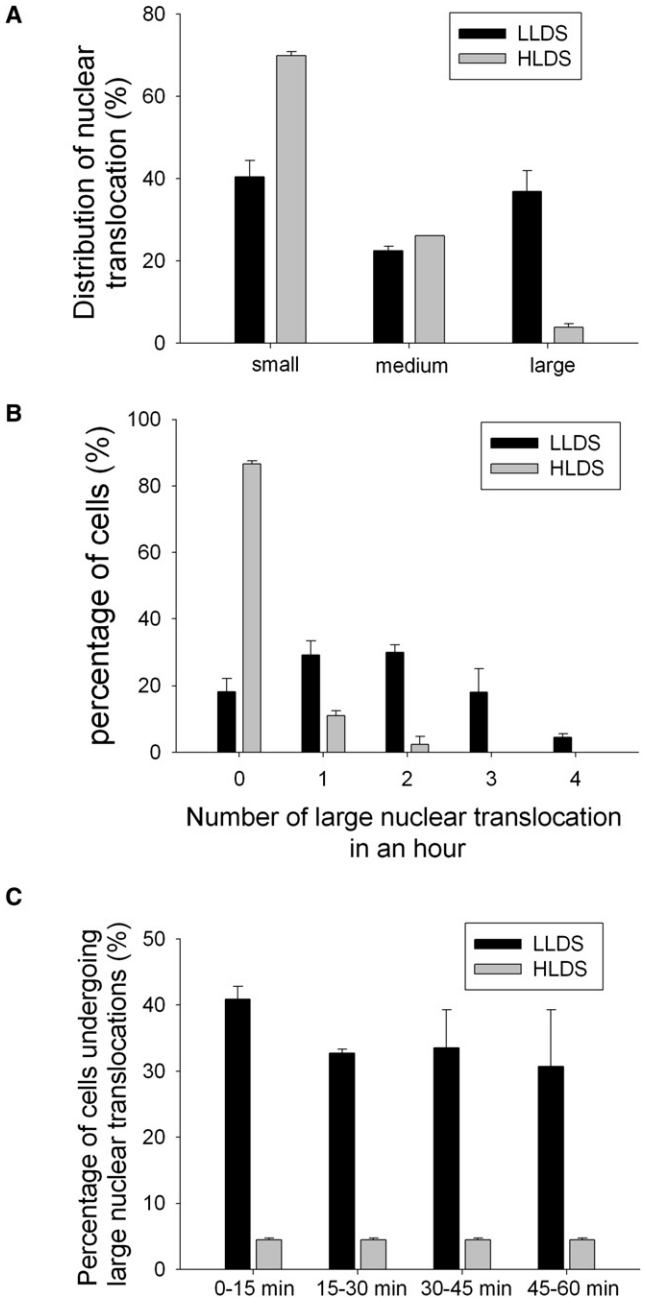

FIGURE 3 Distribution of nuclear translocation as a function of ligand density. (*A*) Magnitude distributions of nuclear translocations in every 15 min interval over 1 h, divided into three groups of different size, large: >10 μm, medium: 5 ~ 10 μm, and small: <5 μm. (*B*) Number distribution of large nuclear translocation for each cell over 1 h, from minimum 0 to maximum 4 in 1 h. (*C*) Time distribution of large nuclear translocation in 15 min interval over 1 h. $n = 26$ and 24 for LLDS and HLDS, respectively. Error bars represent SE.

1.61 ± 0.17 on LLDS and 0.16 ± 0.03 on HLDS. Furthermore, we also tried to determine whether there was a specific time point in the 1 h sequence when the large translocations were most likely to occur. The results are plotted in Fig. 3 *C* where we see that the probability of any cell in the population undergoing a large translocation is the same, within experimental error, for each of the time intervals. These results clearly indicate that: a), Cells do not move continuously on either surface; rather, the cells move in a pulsed manner with short pulse intervals. b), The size of nuclear translocations in a given pulse is a function of the surface ligand density, which in turn regulates the cell polarization and focal adhesion distribution.

Different distribution profiles of nuclear translocations on LLDS and HLDS also suggest that the cellular traction forces redistribute in different ways during cell migration. Thus, we decided to investigate the spatiotemporal redistribution of cellular traction forces on both surfaces within these 15 min intervals, taken over 1 h. In this case, rather than obtaining an ensemble average, we studied individual cells where the traction stress distribution across the cell could be directly correlated with the nuclear translocation, rather than a statistical average.

Traction stress distribution during cell migration imaging cellular traction fields

The substrate deformation induced by cell attachment was analyzed using a previous established DISC technique (23). Fig. 4 *A* shows a displacement vector map generated by a typical migrating cell on LLDS with distinct front and rear ends. The outline of the cell and its nucleus obtained from the differential interference contrast image is superimposed. The resolution of DISC technique is only limited by the resolution of digital images taken by confocal microscope recording the florescent bead distribution, from which displacement data for each pixel point (1024×1024 in this study) can be obtained. Here, vector density is diluted by 1:160 to make the map clear. From the vector map we can see that the largest displacements occur in well-defined loci along the protrusion of the cell, and all the displacements are radially distributed from the nuclear region, which is consistent with previous reports (10).

The DISC results are then input into the FEM model, which calculates the stress and strain fields associated with the given displacements as boundary conditions. We assume that the modulus of the gel is uniform and isotropic, and the stress and strain fields are linearly related. In Fig. 4 *B*, we show the corresponding stress field generated by the cell attachment on LLDS. With high spatial resolution, we imaged where these stresses are applied relative to the cell membrane and the locus of nucleus. Because the cell is not a rigid body, the stresses that are exerted in different subregions can vary greatly. We therefore subdivided the cell into three regions, the front; the nuclear; and the rear, where we found the largest stress concentrations. The traction forces behind leading edge and at trailing edge of the cell are usually known as propulsive and resistant forces (14). Forces in the vicinity of the nucleus have been reported previously (24), but their function has not been known. To determine the role of these forces in the migration of cells,

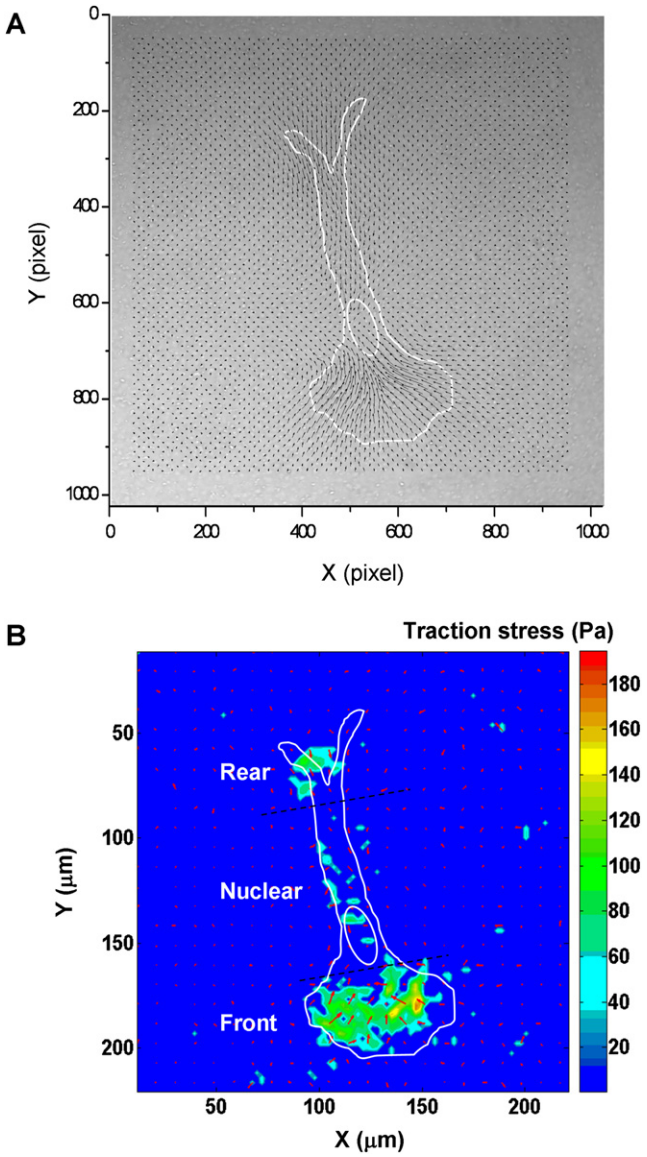

FIGURE 4 (*A*) Vector map determined using DISC technique, representing the displacement generated by a typical migrating cell on LLDS. Vector density is diluted by 1:160 to make the map clear. Arrows show the direction and relative magnitude of the displacement field of the hydrogel surface beneath the attached fibroblast. The phase contrast image from differential interference contrast is superimposed to provide the outline of the cell and its nucleus. (*B*) Traction field calculated by FEM based on the displacement data from DISC. In the color map, arrows show the direction and relative magnitude of the stress field exerted by the attached fibroblast; colors show the absolute magnitude of the stress field in Pa (see *color bar*). Cellular traction stresses concentrate in three distinct regions, the front, the nuclear, and the rear of the cell.

time-sequence data were obtained for each of the different substrates with either LLDS or HLDS.

LLDS

Time sequences of the displacement and traction fields induced by a migrating cell on LLDS are shown in Fig. 5. In each image, the perimeter of the cell and its nucleus are outlined by highlighting the phase contrast images. From this figure, we see that propulsive traction stresses were concentrated behind the cell leading edges along two directions (*a* and *b* in Fig. 5), whereas resistant traction stresses were at the trailing edge (*e* in Fig. 5), which strategically balance the traction stresses at the front. The inset in Fig. 5 is a high-resolution plot of the cell's initial leading edge, where the individual vectors corresponding to the locus of each traction stress are clearly resolved. With high spatial resolution at 0.70 μm determined by the element size in the FEM model, these rearward stresses were shown to localize within a narrow band, no more than 1 ~ 2 μm, positioned ~10 ~ 20 μm behind the leading edge, in agreement with previous reports (9,10,16). However, this traction stress loci at the initial leading edge disappeared 15 min later, which resulted in a retraction of this leading edge, whereas the traction stresses behind the other leading edge enhanced. More interestingly, after 30 min, two loci of traction forces in the perinuclear region appeared. The loci were near the front and the rear edges of the nucleus, respectively (*c* and *d* in Fig. 5).

To determine the role of individual cellular traction forces leading to cell migration, we carefully compared the redistribution of main traction stresses in the five subregions chosen (*a*-*e*) and correlated them to the nuclear translocation occurring during the observation time. The magnitude of the net stresses in each subregion (proportional to the local force) is plotted as a function of time (see Fig. 7 *A*), and the nuclear translocation during the same time (see Fig. 7 *B*). All rearward traction stresses (*a*–*c*) are plotted as being in the positive direction, and the forward resistant traction stresses (*d* and *e*) are plotted as being in the negative direction (see Fig. 7 *A*). It was noticed that the magnitudes of the net stresses at the cell front (*a* and *b*) remained fairly large and increased slowly over time. When the resistant traction stress (*e*) still existed at the trailing edge from $t = 0$ to $t = 15$ min, no nuclear motion was observed. Then, the nucleus moved slightly, to the upper left as a new set of traction stresses (*c* and *d*) were formed around the nucleus at $t = 30$ min, which served as a ''brake'' for the peripheral traction stresses as the stress at the trailing edge of the cell (*e*) decreased. The rearward nuclear traction stress (*c*) at the front edge of the nucleus was relatively small and stable, whereas the forward one (*d*) at the rear edge of the nucleus kept growing to balance the large traction stresses behind the leading edges of the cell (*a* and *b*) instead of the decreasing traction stress at the rear of the cell (*e*), from $t = 30$ min to $t = 60$ min. When the rear traction stress (*e*) was completely dissipated, the tail of the cell retracted at $t = 60$ min. Therefore, the resulting pulse propelled the nucleus to abruptly move forward to the position shown in the last frame, where the equilibrium was reestablished and the cycle would begin again.

The large magnitude of pulsed nuclear translocation is consistent with the high mobility previously measured for

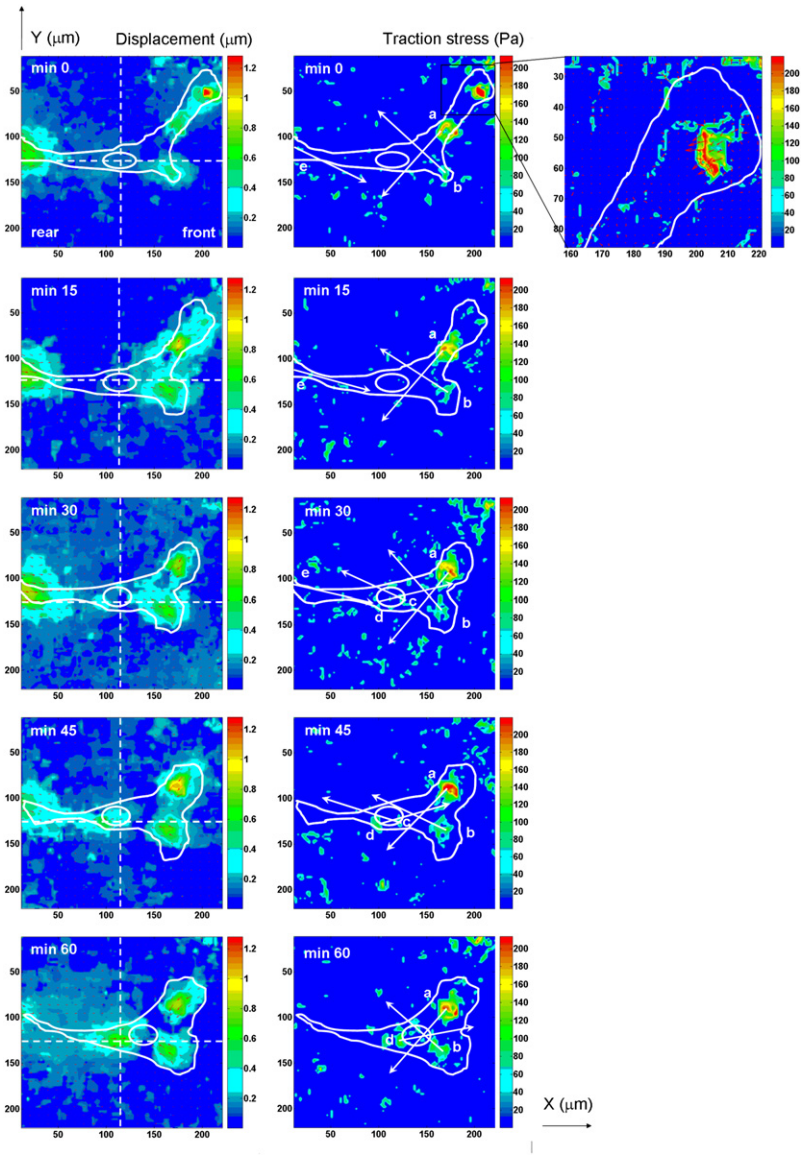

FIGURE 5 Time sequence of displacement and traction fields generated by a migrating fibroblast on LLDS. The left column is displacement maps quantified by DISC. Arrows show the direction and relative magnitude of the displacement field exerted by the attached fibroblast; colors show the absolute magnitude of the displacements in μm (see *color bar*). The intersection of dashed lines shows the initial position of the nucleus. The right column is traction stress distributions obtained from FEM. The directions of net stresses in five subregions exerted by the cell on LLDS are represented by the white arrows, including rearward traction stresses (*a*) and (*b*) behind the leading edges, rearward and forward traction stresses around the front and the rear edges of the nucleus (*c*) and (*d*), and forward traction stress near the trailing edge (*e*). Colors show the absolute magnitude of the stress field in Pa (see *color bar*). (*Inset*) High-resolution image of traction stresses near the initial leading edge.

the cell ensemble on the LLDS. Cells on LLDS presented large nuclear forward-translocations subsequent to retractions of the trailing edge. This phenomenon is accompanied with the relocation of resistant traction stresses from the trailing edge of the cell to the rear edge of the nucleus. These observations clearly demonstrate that the spatiotemporal redistribution of cellular traction stress not only dictates the direction but also the speed of cell migration.

The total stress over the entire cell, proportional to the total net force of the cell, is plotted (see Fig. 7 *C*) together with the mechanical work done by the cell (strain energy) during cell migration for each of the time intervals. From the figure we can see that even though the traction stresses in each subregion vary significantly, the total stress on the cell appears to be constant, because the increase in the positive traction stress at the front of the cell is balanced by the increase in the traction stress at the rear of the nucleus, which acts as a braking force on the cell motion. No obvious correlation can be found between the total stresses with the instantaneous cell motion. Rather, the deformation of individual subregions, each subject to its own set of local stresses, appears to determine the impulse that results in a nuclear translocation. The energy exerted by the cell (or the mechanical work done by the cell) does not occur in a pulsed manner either. From the figure we can see that the total energy exerted by cell in each time interval is constant, which is reasonable considering the time constant of the internal metabolic processes.

It is interesting to note that the nucleus not only undergoes translocations but also deformation. This too can be seen to be a result of the stresses applied in its perimeter. We plot the aspect ratio of the nucleus as a function of time (see Fig. 7 *D*). We can see that the aspect ratio is largest before the nuclear traction stress is generated. Hence the nuclear

deformation arises from stresses pulling the cell in opposite directions at the leading and trailing edges. As the nuclear traction stresses increase, they balance the stresses at the cell perimeter, causing the aspect ratio to decrease and assume a more relaxed shape. After the translocation occurs, the nuclear aspect ratio reaches its smallest point. Because the translocation is also associated with a complex sequence of events resulting in the retraction of the rear segment of the cell, it is possible that the nuclear deformation may have initiated the signaling pathways, which regulate the distribution of the traction forces.

HLDS

In the section of cell migration on HA/FNfds substrates with different ligand densities, we established that the ligand density of the susbstrate determined the average migration speed. We showed in Fig. 1 *A* that the migration speed on the LLDS was nearly three times larger than on the HLDS. Although the cell area was somewhat larger on the HLDS, the aspect ratio was much smaller. To understand the relationship between the ligand density and these effects, we also measured the cellular traction redistribution on HLDS. The displacements and traction fields generated by a typical migrating cell on the HLDS are shown in Fig. 6. In this case, we see that the cell appearance is triangulated with large traction stresses behind two leading edges (*a* and *b* in Fig. 6) and at the cell rear (as *e* in Fig. 6). In addition, traction stresses are also present on opposite sides of the nucleus (*c* and *d* in Fig. 6) at all times. From the figure we can see that the amplitude of the traction stresses and the displacements are approximately twice as large on the HLDS as on the LLDS, which is consistent with the twofold increase in ligand density of the substrates.

During migration, the forward traction stress at the nuclear rear edge (*d*) still gradually replaced the rear traction stress (*e*) and worked as a regulator to control the nuclear translocation similar to LLDS as shown in Fig. 7 *A*. However, this relocation from the rear of cell to the rear edge of the nucleus seemed to take a much longer time on the HLDS, probably due to the higher magnitude of traction stresses. Within the 1 h observation time, these nuclear traction stresses are fairly balanced by the other traction stresses around the cell periphery and therefore the shape of the cell remains symmetric. The major consequence of the symmetric arrangement of the traction stresses is the small amplitude of the nuclear translocation (Fig. 7 *B*). These observations are consistent with previous reports that rear retraction is dominant limitation for cell migration on a highly adhesive surface (25) and clearly explain why the overall cell mobility is much slower on HLDS from a mechanical point of view.

The total stress over the entire cell and mechanical work (strain energy) done by the cell during migration are plotted in Fig. 7 *C* as a function of time. In contrast to the cells on LLDS, we find that the total stress on HLDS is smaller even though the magnitudes of the local stresses are nearly an order of magnitude higher. The distribution of the stresses on the other hand, is far more balanced on HLDS, as can be seen from Figs. 1 and 2, because their aspect ratios are smaller and there are more focal adhesions distributed over a broader area. This is also reflected in the mechanical work done by the cell (strain energy), which is much higher on HLDS than on LLDS. Hence we can see that the work done on a substrate is mostly a function of cell-substrate adhesion rather than the actual motion of the cells.

In Fig. 7 *D*, we also plot the aspect ratio of the nucleus at different times for the cell migrating on the HLDS. From the figure we can see that the ratio is much smaller than on the LLDS and remains fairly constant through the motion cycle. The small deformation of the nucleus is consistent with the presence of the large nuclear traction stress and the much smaller nuclear translocation observed on these surfaces.

Traction stress gradient

In Fig. 8 *A*, we show three-dimensional plots of the initial traction stress gradient for the cells on the LLDS and the HLDS. From the figure we can see that the individual stresses on the HLLDS are much larger than on the LLDS. However, those on the LLDS are weighted toward the front of the cell. Furthermore, the cell morphology is more elongated, enhancing the polarity of the cell. Three randomly selected cells on each substrate were analyzed in this manner, with very similar results. In Fig. 8, *B* and *C*, we plot the mechanical work done by the cell and the total nuclear translocation over 1 h observation period on each surface, averaged for the three cells studied. The translocations observed are consistent with those shown previously for the larger cell ensemble in Fig. 1 *A*. From the figure we see that it is not the cell-substrate adhesion but the traction gradient across the entire cell that directly determines the cell mobility.

The event that triggers the nuclear translocation of the cells on both surfaces is the detachment of the cell rear (25), and the relocation of the stresses from the rear of cell to the vicinity of the nucleus. In Fig. 9, we plot the ratio between the rear traction stresses and the nuclear rear traction stresses obtained over the observation period for individual cells on each surface described above. We find that the ratio is significantly larger at the beginning on the LLDS than on the HLDS and decreases in a much faster way, finally achieving zero at the end of the observation period. The change in the stress gradient at the rear section of the cells is clearly correlated with the impulse that results in the nuclear translocation in each case. The maximal net stresses at rear and nuclear rear and the ratio between them are presented for three cells on each substrate in Table 1. The maximal net stresses at rear and nuclear rear are comparable for each cell. The ratio between them is >0.8 on both substrates. This shows that although individual cells are different in their size, shape, and traction distribution, the

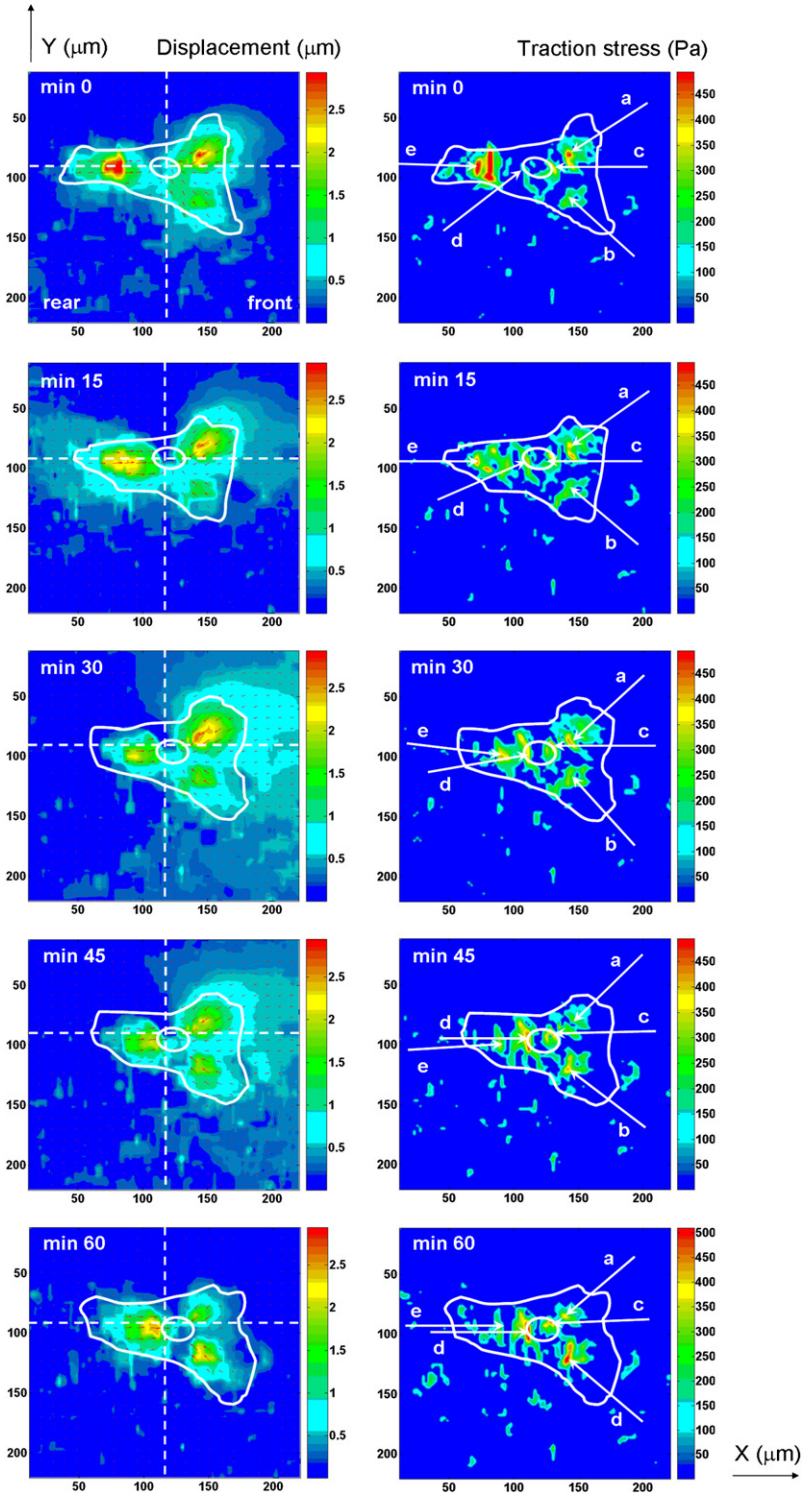

FIGURE 6 Time sequence of displacement and traction fields generated by a migrating fibroblast on HLDS. The left and right columns are displacement maps and traction fields calculated by DISC and FEM, respectively. Arrows in displacement maps show the direction and relative magnitude of the displacement field exerted by the attached fibroblast; colors show the absolute magnitude of the displacements in μm (see *color bar*). The intersection of dashed lines in displacement maps shows the initial position of the nucleus. White arrows *a-e* in traction field indicate directions of net stress in five subregions similar to those in LLDS. Colors in traction fields show the absolute magnitude of the stress field in Pa (see *color bar*).

replacement of traction stresses from the cell rear to the posterior end of the nucleus is always observed.

DISCUSSION

We developed what to our knowledge is a new system to image the spatiotemporal redistribution of cellular traction stresses during cell migration. The techniques of DISC combined with FEM, which have long been used to analyze mechanical defects of materials, were successfully applied to the dynamic measurement of cellular traction stresses. We designed a physiologically relevant ECM mimic, HA/FNfds hydrogel, and produced gels with a controlled modulus that allowed cells to generate a clear distribution of cellular

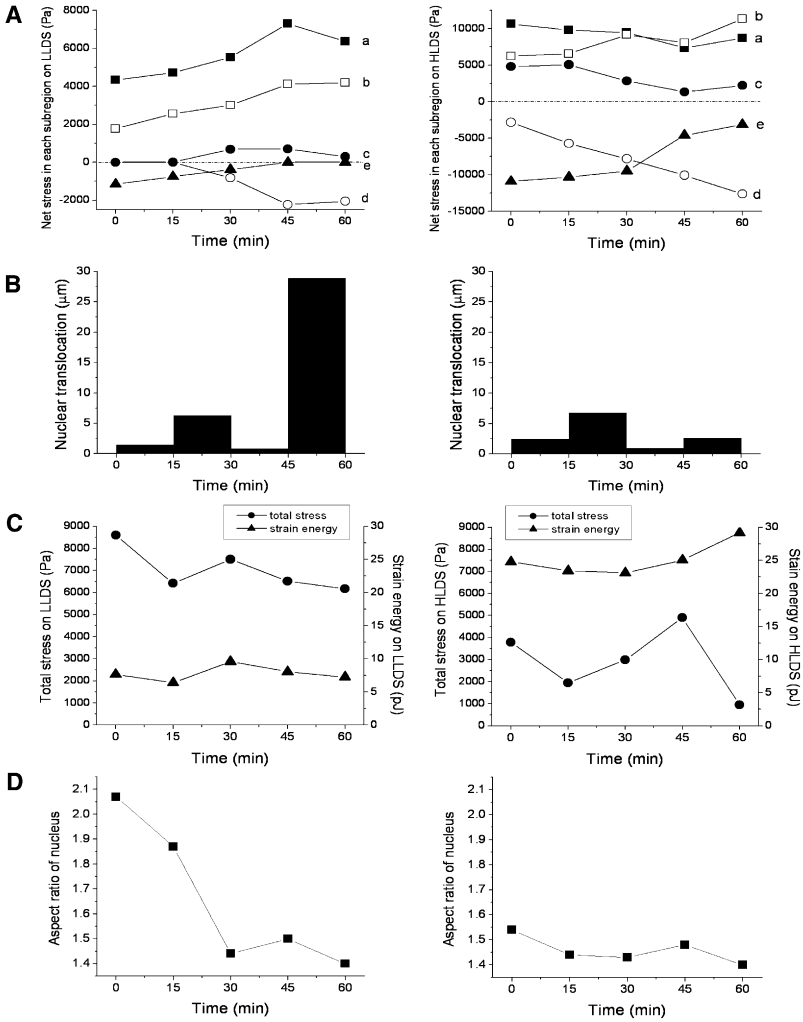

FIGURE 7 *A* and *B* are the temporal redistribution of net stresses in each subregion and corresponding nuclear translocation on LLDS and HLDS. Net stresses in the five subregions (*a-e* in Figs. 5 and 6) are plotted as a function of time for either LLDS (*left*) or HLDS (*right*) in *A*, where ±, respectively, denotes rearward and forward stresses, which propel or resist forward motion. Nuclear translocation distances in every 15 min interval are plotted as a function of time for either LLDS (*left*) or HLDS (*right*) in *B*. (*C*) Total net stress and mechanical work done by the cell evaluated by stain energy stored in the substrate are plotted as a function of time for either LLDS (*left*) or HLDS (*right*). (*D*) Aspect ratio of the nucleus as a function of time for either LLDS (*left*) or HLDS (*right*).

traction stresses. We then imaged the sequence of these traction stresses during cell migration and compared the process on substrates with different ligand density and cell adhesion. We found that fibroblast migration is a discontinuous process that occurs when a small imbalance of the local traction stresses occurs. We showed that cell migration is the result of a spatiotemporal redistribution of cellular traction stresses, which readjust themselves continuously to maintain a constant total net stress. Motion occurs in a pulsed manner, when a large relocation of the stresses, from the rear to the nucleus of the cells occurs. The sequence was similar on both LLDS and HLDS, but the magnitude of the pulses was found to correlate with the ligand density and the cell-substrate adhesion.

Our results showed that migrating cells are always polarized along certain directions with clear front and rear. Several loci of strong traction stresses are observed at the leading edge, which are invariably balanced by a concerted locus at the rear of the cell. Preparation of motion is usually signaled by a decrease in the magnitude of the rear stresses. A new set of traction stresses is then observed to arise in the nuclear region, which grows proportionally to the decrease of the rear traction stresses and mainly along the same direction. This braking force prevents cell imbalance and motion. As the rear traction stresses decrease, a point is reached where the rear region becomes completely detached from the substrate and contracts. At this point, the rear traction is seen to abruptly disappear and a momentary imbalance in the traction forces occurs. This results in an imposed force to the cell, inducing a forward motion of the nucleus. The motion stops as the nuclear braking force increases even further to completely balance the front traction forces. The front of the cell then moves forward and the cycle begins again. When the ligand density is increased on the hydrogel, the cell-substrate adhesion is enhanced and much stronger traction forces form. The sequence of events is similar, but complete release of the rear edge is more difficult to achieve and takes longer. Consequently, the total motion of the cell is slower. These results support a recent model predicting that adhesion/contraction would directly regulate the migration speed of cells across matrices of different ligand densities (26).

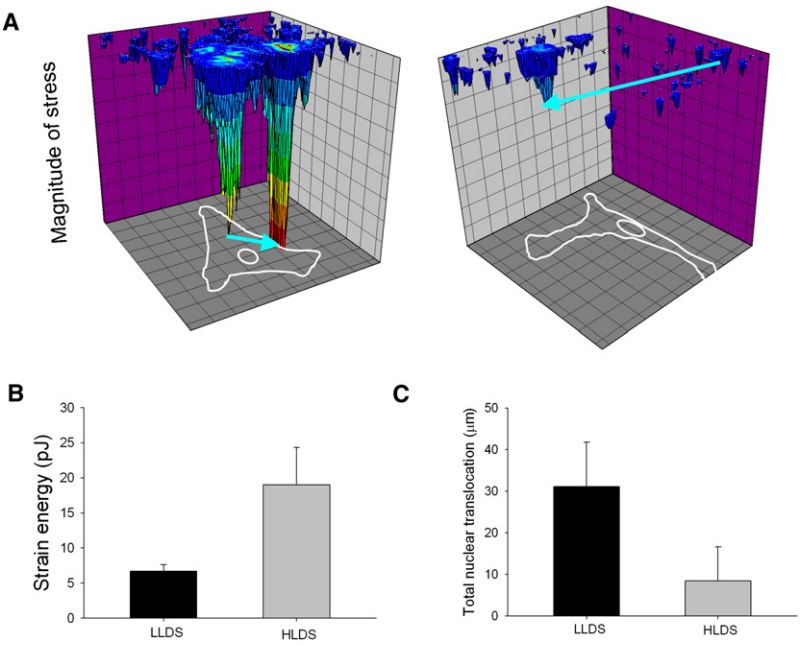

FIGURE 8 (*A*) Magnitude distributions of cellular traction stresses on LLDS and HLDS plotted in three-dimension. The blue arrows show the traction gradients across the entire cells. *B* and *C* are the average mechanical work done by the cell and total nuclear translocation over 1 h observation period on LLDS and HLDS, averaged from three cells. Error bars represent SD.

Compared with previous studies, we found that the appearance of traction stresses around nuclei plays an important role to replace the resistant traction at the rear and maintain a relatively steady movement of the entire cell body. Furthermore, we demonstrated that it is the redistribution of cellular traction stresses occurring among three discrete mechanical regions, the front, the rear, and the nuclear region, rather than total traction stress across the entire cell that leads to the pulsed manner of cell migration. This implied that although a cell can not be treated like a solid object, its behavior can still be explained by the net stresses in each subregion. Regardless of the magnitude of the traction stresses, which is proportional to the ligand density, cells move faster when cellular tractions show clear asymmetry across the whole cell, as in the case of LLDS. Large nuclear translocation only occurred on LLDS where the rear traction forces are completely relocated around the nuclear region. The relocation of tractions from the rear of the cell to the nuclear region also happened on HLDS, but it was slower due to the high magnitude of traction stresses. This provides a mechanical explanation of why cells migrate faster and in a clear pulsed manner on LLDS compared to HLDS. In addition to the redistribution of cellular traction stresses, we also noticed that, as the rear detached, the shape of nuclei changed from being ellipsoidal to circular. Such nuclear distortion may relate to the structural reorganization of nuclei (27) in response to the overall redistribution of cellular traction stresses. Together with dynamics of cytoskeleton and adhesion molecules, these cellular mechanical changes may stimulate cell migration in certain signaling pathway (28).

Based on all the detailed results, we proposed a traction gradient foreshortening model for fibroblast migration. As shown in Fig. 10, a large nuclear translocation occurs when rear traction forces are relocated to a posterior nuclear

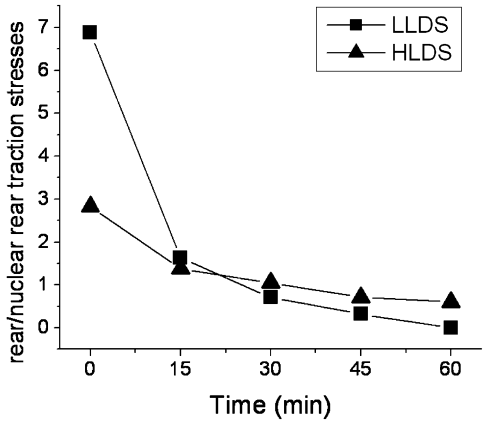

FIGURE 9 Ratio of the net rear stress to the net nuclear rear stress as a function of time.

TABLE 1 Maximal rear stresses and maximal nuclear rear stresses for three individual cells on LLDS and HLDS

Cell number on LLDS	Maximal net stress at rear (σ_{rear}/Pa)	Maximal net stress at nuclear rear ($\sigma_{nuclear}$/Pa)	Ratio of $\sigma_{rear}/\sigma_{nuclear}$
1	5.3×10^2	1.1×10^3	0.48
2	4.9×10^2	6.1×10^2	0.80
3	1.4×10^3	1.0×10^3	1.4
Mean	8.1×10^2	9.0×10^2	0.89
SD	5.1×10^2	2.6×10^2	0.46
Cell number on HLDS			
1	1.2×10^4	1.7×10^4	0.70
2	4.8×10^3	8.1×10^3	0.59
3	2.5×10^4	2.1×10^4	1.2
Mean	1.4×10^4	1.5×10^4	0.83
SD	1.0×10^4	6.6×10^3	0.32

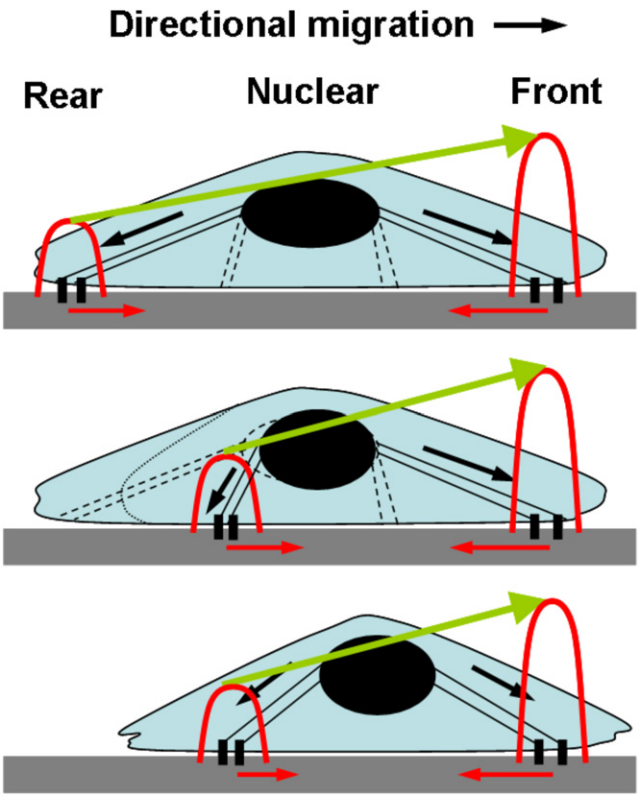

FIGURE 10 Traction gradient foreshortening model for fibroblast migration. The cell stretches out when the parallel stress fibers pull laterally on the confined nucleus from both front and rear sides, inducing the nuclear elongation. As the focal adhesions slide from the cell rear to the nuclear rear, the rear traction stresses relocate at a posterior nuclear location, resulting in the relaxation and translocation of the nucleus. Red arrows show the traction stresses exerted on the substrate through focal adhesions, and red curves show their magnitude. The green arrow shows the traction gradient across the cell, which becomes shorter as the rear traction stresses relocate around the nucleus.

location with concomitant foreshortening of the traction gradient across the cell. This process likely relates to the reorganization of the cytoskeleton, transmembrane adhesion molecules, and the nucleus (29). More focal adhesions slide toward the nucleus from the rear (5) and the nucleus become less elongated. Our results suggested that the reinforcing of tractions around the nucleus is another critical step in fibroblast migration besides the active propulsive tractions behind the leading edges and passive resistance at the trailing edges (14).

This traction gradient foreshortening model revealed where fibroblasts reload the rear forces during cell migration, which does not contradict the previous cell migration models, such as the frontal towing model (24), but further refines those models. Traction mapping around the nuclear region had, in fact, been shown previously when Munevar et al. (24) presented the color rendering of the normalized shear of a migrating normal 3T3 fibroblast. However, it has failed to receive widespread attention, probably due to the lack of an exhaustive temporal dynamics of traction during cell migration. We have addressed these concerns in this study by obtaining high-resolution mapping of the spatiotemporal dynamics of both cellular and nuclear tractions and correlating them with cell motility. Our results are also consistent with previous qualitative studies that report the dynamics of focal adhesions during cell migration, which remain stationary at the leading edge while sliding toward the nucleus at the rear end (5,6). Our rigorous quantitative analysis suggests that the focal adhesion motility (toward the nucleus) observed at the rear end of a migrating cell correlates with the relocation of traction stresses from cell rear to a posterior nuclear location. Notably, we find that traction forces at the cell's leading edge remain unchanged, again in agreement with the observed stationary phenotype of focal adhesions at that location (5,6). Our results highlight the importance of the perinuclear region during cell migration, which should be considered more carefully in future studies. The sensing mechanism that determines the distribution of nuclear traction stresses may also play a role in nuclear function during mechnotransduction (29) and a number of other molecular events associated with cell migration (30).

This measuring system also affords a tool for detailed study of the effects of other pathological factors on cell migration such as diabetes, which affect the chemistry of the binding ligands or the processes regulating focal adhesion assembly. The easily controlled spatial resolution, as illustrated by the inset in Fig. 5, indicates that this is a promising method to measure the traction forces when cells are cultured on a surface with submicron-scale resolution, such as the electrospun three-dimensional nanofibrous scaffolds (31) that better mimics the natural ECM architecture. The cells themselves can also be included in the FEM model with further understanding of their mechanical properties.

SUPPORTING MATERIAL

A figure is available at http://www.biophysj.org/biophysj/supplemental/S0006-3495(09)00601-8.

We thank Dr. Xiangdong Ren for the cloning of FNfds, and Prof. Glenn D. Prestwich and Dr. Xiao Zheng Shu for providing HA-DTPH and sharing the chemistry to obtain cross-linked HA hydrogels.

This work was supported by grants from the National Science Foundation for the Materials Research Science and Engineering Center program to M.R., and from the National Institutes of Health/NA10143 Merit Award and Armed Forces Institute of Regenerative Medicine Award to R.A.F.C.

REFERENCES

1. Lauffenburger, D., and A. Horwitz. 1996. Cell migration: a physically integrated molecular process. *Cell*. 84:359–369.
2. Mitchison, T., and L. Cramer. 1996. Actin-based cell motility and cell locomotion. *Cell*. 84:371–379.
3. Sheetz, M., D. Felsenfeld, and C. Galbraith. 1998. Cell migration: regulation of force on extracellular-matrix-integrin complexes. *Trends Cell Biol*. 8:51–54.

4. Geiger, B., and A. Bershadsky. 2001. Assembly and mechanosensory function of focal contacts. *Curr. Opin. Cell Biol.* 13:584–592.

5. Smilenov, L. B., A. Mikhailov, R. J. Pelham, E. E. Marcantonio, and G. G. Gundersen. 1999. Focal adhesion motility revealed in stationary fibroblasts. *Science.* 286:1172–1174.

6. Wehrle-Haller, B., and B. A. Imhof. 2003. Actin, microtubules and focal adhesion dynamics during cell migration. *Int. J. Biochem. Cell Biol.* 35:39–50.

7. Beningo, K., and Y. Wang. 2002. Flexible substrata for the detection of cellular traction forces. *Trends Cell Biol.* 12:79–84.

8. Dembo, M., T. Oliver, A. Ishihara, and K. Jacobson. 1996. Imaging the traction stresses exerted by locomoting cells with the elastic substratum method. *Biophys. J.* 70:2008–2022.

9. Dembo, M., and Y. Wang. 1999. Stresses at the cell-to-substrate interface during locomotion of fibroblasts. *Biophys. J.* 76:2307–2316.

10. Pelham, R., and Y. Wang. 1999. High resolution detection of mechanical forces exerted by locomoting fibroblasts on the substrate. *Mol. Biol. Cell.* 10:935–945.

11. Tan, J., J. Tien, D. Pirone, D. Gray, K. Bhadriraju, et al. 2003. Cells lying on a bed of microneedles: an approach to isolate mechanical force. *Proc. Natl. Acad. Sci. USA.* 100:1484–1489.

12. Buguin, A., P. Chavrier, B. Ladoux, O. du Roure, A. Saez, et al. 2005. An array of microfabricated pillars to study cell migration. *Med. Sci. (Paris).* 21:765–767.

13. Pelham, R. J., and Y. L. Wang. 1997. Cell locomotion and focal adhesions are regulated by substrate flexibility. *Proc. Natl. Acad. Sci. USA.* 94:13661–13665.

14. Munevar, S., Y. Wang, and M. Dembo. 2001. Distinct roles of frontal and rear cell-substrate adhesions in fibroblast migration. *Mol. Biol. Cell.* 12:3947–3954.

15. du Roure, O., A. Saez, A. Buguin, R. Austin, P. Chavrier, et al. 2005. Force mapping in epithelial cell migration. *Proc. Natl. Acad. Sci. USA.* 102:2390–2395.

16. Harris, A., P. Wild, and D. Stopak. 1980. Silicone-rubber substrata. New wrinkle in the study of cell locomotion. *Science.* 208:177–179.

17. Ghosh, K., Z. Pan, E. Guan, S. Ge, Y. Liu, et al. 2007. Cell adaptation to a physiologically relevant ECM mimic with different viscoelastic properties. *Biomaterials.* 28:671–679.

18. Ghosh, K., X. Ren, X. Shu, G. Prestwich, and R. Clark. 2006. Fibronectin functional domains coupled to hyaluronan stimulate adult human dermal fibroblast responses critical for wound healing. *Tissue Eng.* 12:601–613.

19. Palecek, S., J. Loftus, M. Ginsberg, D. Lauffenburger, and A. Horwitz. 1997. Integrin-ligand binding properties govern cell migration speed through cell-substratum adhesiveness. *Nature.* 385:537–540.

20. Engler, A., L. Bacakova, C. Newman, A. Hategan, M. Griffin, et al. 2004. Substrate compliance versus ligand density in cell on gel responses. *Biophys. J.* 86:617–628.

21. Ghosh, K., X. Shu, R. Mou, J. Lombardi, G. Prestwich, et al. 2005. Rheological characterization of in situ cross-linkable hyaluronan hydrogels. *Biomacromolecules.* 6:2857–2865.

22. Clark, R., J. An, D. Greiling, A. Khan, and J. Schwarzbauer. 2003. Fibroblast migration on fibronectin requires three distinct functional domains. *J. Invest. Dermatol.* 121:695–705.

23. Guan, E., S. Smilow, M. Rafailovich, and J. Sokolov. 2004. Determining the mechanical properties of rat skin with digital image speckle correlation. *Dermatology.* 208:112–119.

24. Munevar, S., Y. Wang, and M. Dembo. 2001. Traction force microscopy of migrating normal and H-ras transformed 3T3 fibroblasts. *Biophys. J.* 80:1744–1757.

25. Palecek, S., A. Huttenlocher, A. Horwitz, and D. Lauffenburger. 1998. Physical and biochemical regulation of integrin release during rear detachment of migrating cells. *J. Cell Sci.* 111:929–940.

26. Hautaniemi, S., S. Kharait, A. Iwabu, A. Wells, and D. A. Lauffenburger. 2005. Modeling of signal-response cascades using decision tree analysis. *Bioinformatics.* 21:2027–2035.

27. Dahl, K. N., A. J. Engler, J. D. Pajerowski, and D. E. Discher. 2005. Power-law rheology of isolated nuclei with deformation mapping of nuclear substructures. *Biophys. J.* 89:2855–2864.

28. Ingber, D. E. 2003. Mechanosensation through integrins: cells act locally but think globally. *Proc. Natl. Acad. Sci. USA.* 100:1472–1474.

29. Maniotis, A., C. Chen, and D. Ingber. 1997. Demonstration of mechanical connections between integrins cytoskeletal filaments, and nucleoplasm that stabilize nuclear structure. *Proc. Natl. Acad. Sci. USA.* 94:849–854.

30. Ridley, A., M. Schwartz, K. Burridge, R. Firtel, M. Ginsberg, et al. 2003. Cell migration: integrating signals from front to back. *Science.* 302:1704–1709.

31. Ji, Y., K. Ghosh, X. Shu, B. Li, J. Sokolov, et al. 2006. Electrospun three-dimensional hyaluronic acid nanofibrous scaffolds. *Biomaterials.* 27:3782–3792.